Experiments in Fluids 29 [Suppl.] S129–S140 © Springer-Verlag 2000

Combined planar laser-induced fluorescence–particle image velocimetry technique for velocity and temperature fields

K. Hishida, J. Sakakibara

Abstract Combined use of particle image velocimetry (PIV) with planar laser-induced fluorescence (PLIF) was developed to measure both velocity and scalars such as temperature and concentration in thermo-fluid flow. PLIF, which uses a temperature-sensitive fluorescent dye excited by a laser light sheet, is a whole-field temperature diagnostic. The technique was applied to a thermal stratified flow and a plane impinging jet. The time evolutions of vortical and thermal structures were successfully obtained in order to understand the mechanism of the turbulent heat transfer in these flows.

1 Introduction

Heat transfer is, of course, one of the major subjects of thermo-fluid engineering ranging from micro-scale heat flows in electronic devices to geophysical flows such as atmospheric/oceanic flows. If the flow is turbulent, the net flow of heat is transferred by convection rather than conduction. The convection of heat, represented by turbulent heat flux $u_i t_j$, is the key to understanding such a flow. Especially, the production term of the transport equation of turbulent energy might be modeled to close the equation as far as one would perform Reynolds averaged numerical simulation. In modeling this term, the experimental data of turbulent heat flux $u_i t_j$ is always necessary, although measurement of the turbulent heat flux is still not easy because the velocity and temperature must be measured at the same point and time.

In this paper, we present a new technique of measuring the turbulent heat flux based on simultaneous use of particle image velocimetry (PIV) and planar laser-induced fluorescence (PLIF) to measure both velocity and temperature. In PLIF, the fluorescence intensity is proportional to the exciting light intensity and the concentration of the fluorescent dye. For some dyes, e.g. Rhodamine B (RhB), the fluorescence intensity depends on the temperature. This characteristic can be used to measure the temperature of the solvent if one can keep both the concentration and the exciting light intensity constant. PLIF can be combined with conventional PIV to achieve simultaneous measurement of temperature and velocity and its cross-product, the turbulent heat flux. Here, fluorescent dye and tracer particles are mixed in the flow, and two CCD cameras, one for PLIF and the other for PIV, are used at a same time to image both the fluorescent intensity and particles' scattering. This combined technique has been applied to clarify the heat transfer and turbulent characteristics of the stratified flow, the natural convection and the plane impinging jet.

K. Hishida (✉)
Department of System Design Engineering,
Keio University, Yokohama, Japan 223-8522

J. Sakakibara
Institute of Engineering Mechanics and Systems,
University of Tsukuba, Tsukuba, Japan 305-8573

2 Technical basics

2.1 PLIF for temperature measurement

Various techniques have been used previously to obtain the spatial distribution of the temperature in water. Thermo-chromic liquid crystals (TLC) are commonly used to visualize temperature qualitatively, and several researchers have reported quantitative measurements (Akino et al. 1988; Dabiri and Gharib 1991; Fujisawa et al. 1997). It is now possible to obtain quite sensitive TLC particles which change color from red to blue in a range of 1 K or less. However, the accuracy relative to the measurement range is not still large. The uncertainty is approximately 0.1 K, with an available measurement range of 0.7 K.

Instead of using TLC particles, temperature-sensitive fluorescent dyes excited by laser light can alternatively be used as a molecular marker representing temperature of solution of the dyes. This technique, called laser-induced fluorescence (LIF), has been widely used to measure the species concentration and temperature of gas flames (Hanson 1986; Joklik et al. 1991), scalar concentration and diffusion process of dyes in liquid (Dahm et al. 1991) and three-dimensional velocity by solving scalar transport equation (Dahm et al. 1992). Temperature measurement of a liquid was applied by Nakajima et al. (1990) by combining LIF with conventional laser Doppler velocimetry (LDV) to achieve simultaneous measurement of velocity and temperature at one point. Nakajima's work has been extended to planer temperature measurements using PLIF and PIV (Sakakibara et al. 1993; 1997; Sato et al. 1997).

The fluorescence intensity I emitted from a unit volume is defined as

$$I = I_0 C \phi \varepsilon \qquad (1)$$

where I_0 is the incident light flux, C is the concentration of the dye solution, ϕ is the quantum efficiency, ε is an absorption coefficient. We assume that C is small enough to ignore the attenuation of the light as it passes through the medium. In most organic dyes, the quantum efficiency ϕ is temperature dependent. The change in fluorescence intensity is normally small, on the order of 1% per K. However, the sensitivity of some compounds such as RhB can be as high as 2% K^{-1}. In contrast, the absorption coefficient ε does not have significant temperature dependency. Thus, it is possible to measure the temperature of the solution keeping the incident light flux I_0 and concentration C constant.

The temperature variation of the fluorescence intensity of RhB (5.0×10^{-2} mgl^{-1}), I_{RhB}, is shown in Fig. 1. The intensity is normalized by the value at $T = 20$ °C. The intensity change of RhB is quite repeatable and significant, especially at lower temperatures. The temperature dependence of RhB is 2.3% K^{-1} at 20 °C.

The relationship between temperature and the quantum efficiency ϕ of RhB was obtained from values at $T = 20$ °C as follows:

$$\phi(T) = \phi(= 20\ ^\circ\mathrm{C})\frac{I(T)}{I(T = 20\ ^\circ\mathrm{C})} \tag{2}$$

Here, an absolute value of ϕ ($T = 20$ °C) is 0.31 for RhB, as reported by Arbeloa et al. (1991). Note that the temperature dependence of the absorption coefficient is less than 0.05% K^{-1}. The function $\phi(T)$ is approximated to be a second-order polynomial by applying the least-square method to the experimental data on the right-hand side of Eq. (2).

If the exciting light intensity I_0 and concentration C are kept constant in time, but not necessarily in space, a fluorescence intensity at a point detected by the camera, $I_{mes} = I + I_b$, normalized by a reference intensity at the same point, $I_{ref} = I(T_{ref} + I_b)$, at a reference temperature T_{ref} is expressed as follows, based on Eq. (1) and $\phi(T)$:

$$\frac{I_{mes} - I_b}{I_{ref} - I_b} = \frac{I(T)}{I(T_{ref})} = \frac{\phi(T)}{\phi(T_{ref})} \tag{3}$$

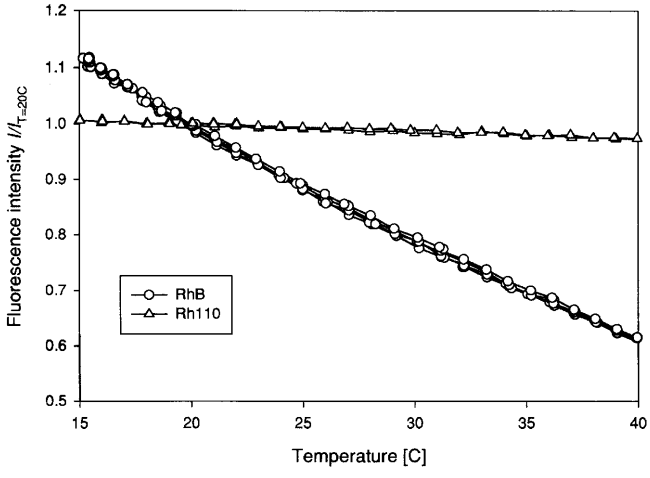

Fig. 1. Variation in the fluorescence intensity against temperature

In the above equation, I_b denotes background intensity of that point measured without excitation light. Temperature to be measured is, therefore, expressed as

$$T = \phi^{-1}\left(\frac{I_{mes} - I_b}{I_{ref} - I_b}\phi(T_{ref})\right) \tag{4}$$

In practice, I_{ref}, T_{ref} and I_b must be measured on site prior to the actual measurement, while keeping the temperature of the flow field uniform.

2.2 Two-color PLIF

Regarding PLIF in the previous section, it was necessary to keep the excitation intensity I_0 constant. However, in many situations, I_0 can be affected by various factors including the refraction of the light passing through the thermal field. In order to avoid this problem, it is necessary to provide a means of measuring the local, instantaneous intensity of the illuminating light. This can be done using the emission intensity of a fluorescent dye that is not sensitive to temperature. This leads to the use of a mixture of two fluorescent dyes RhB and Rhodamine 110 (Rh110) which have different temperature dependences and different emission spectra, as shown in Fig. 1 and Table 1. Details of this technique are described in an original manuscript by Sakakibara and Adrian (1999).

Suppose each emission spectrum can be perfectly separated by beam-splitting optics as shown in Fig. 2, then the individual intensities can be measured by two different cameras α and β, whose voltage outputs are V^α and V^β, respectively. The ratio

$$\frac{V^\alpha}{V^\beta} = \frac{I_{RhB}}{I_{Rh110}} = \frac{C_{RhB}\phi_{RhB}\varepsilon_{RhB}}{C_{Rh110}\phi_{Rh110}\varepsilon_{Rh110}} \tag{5}$$

is independent of the incident light flux I_0, but it can be a function of temperature. In practice, imperfect separation of I_{RhB} and I_{Rh110} arises from the overlap of the emission spectrum of the two fluorescent dyes, and some fraction of I_{RhB} is detected by camera β, and some fraction of I_{Rh110} is detected by camera α. This could be accounted for by a proper calibration procedure. Application of two-color PLIF is described in Sect. 3.2.

2.3 Combined PLIF–PIV

Simultaneous use of PLIF and PIV enables us to measure an instantaneous and two-dimensional velocity and temperature distribution in water. Figure 3 shows an example of the measurement system used in the experiments described in Sects. 3.1 and 3.3. The continuous laser light beam was switched by an acoustic optical module (AOM) to control the exposure time, and introduced into the optical fiber and light sheet optics. Exposure time was typically 1 ms in our experiments. Two cameras and image capturing systems are necessary to detect particle images and fluorescence images independently. Here, the one camera for the fluorescence image has to cut the scattering light from the PIV particles by attaching an optical filter in front of the camera. Typically, the filter would be a short-wavelength-cut type, since the excitation wavelength is

Table 1. Basic characteristics of RhB and Rh110

Dye	Molecular weight	λ_{abs} [nm]	λ_{ems} [nm]	ϕ	$\varepsilon_{\lambda=488}$ [m^2/g]	$\varepsilon_{\lambda=\lambda_{RhB}}$ [m^2/g]	$\varepsilon_{\lambda=\lambda_{Rh110}}$ [m^2/g]
RhB	479.02 (Jones 1990)	554	575	0.31 (Arbeloa et al. 1991)	4.4	1.1	5.8
Rh110	366.80 (Jones 1990)	496	520	0.8	34	0.073	1.1

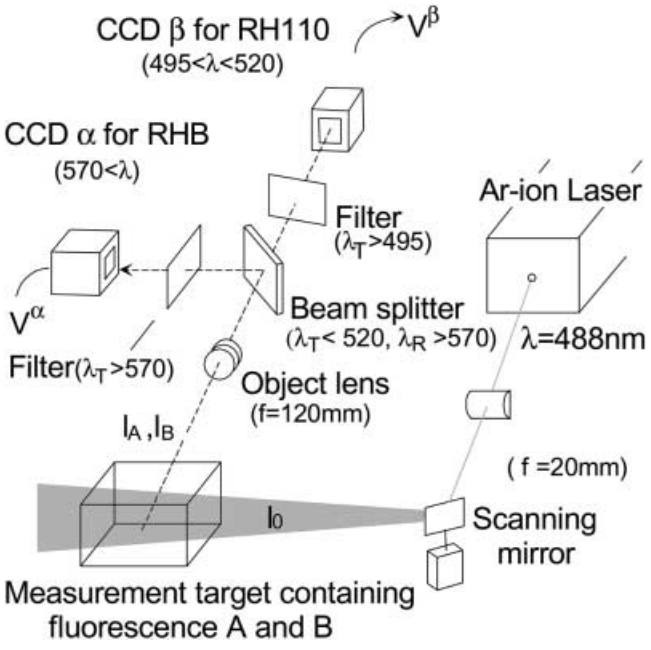

Fig. 2. Arrangement of optical component

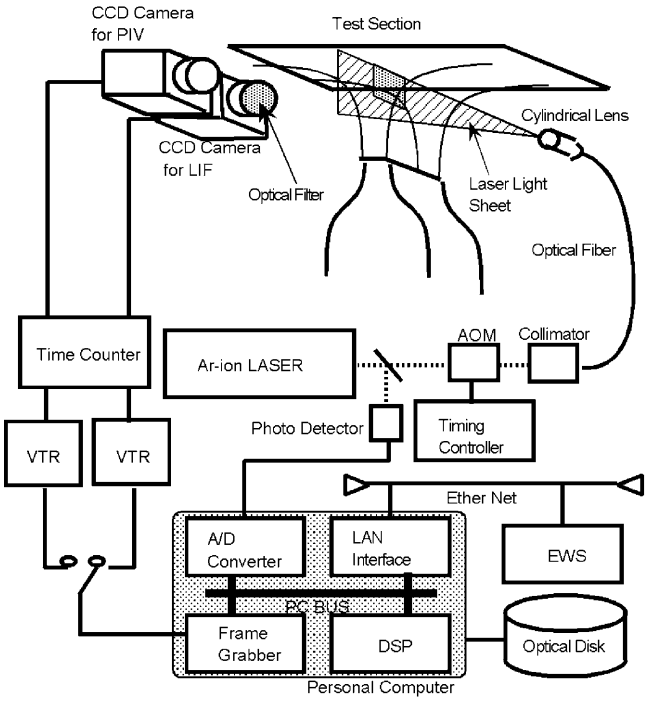

Fig. 3. Block diagram of combined PIV/PLIF system

shorter than the emission wavelength. Although the short-wavelength-cut filter could prevent particle scattering light considerably (>99.9%), it still might not be perfect. Furthermore, volumes of fluorescent dye replaced by the tracer particle may reduce the fluorescence intensity observed.

To detect both PIV and PLIF images at the same time and same location, two cameras must be synchronized in time and space. The former can be done by, for example, triggering two CCD cameras at a same time, or connecting the video signal of one camera into a synchronization input of the other camera for conventional RS-170 CCD cameras. The latter is basically to adjust both cameras to look at same location precisely. It is, however, fairly difficult to overlap a view region of one camera to that of the other by adjusting the magnification and axis of the camera optics. Instead of making both cameras look at the same location, an alternative way is a position calibration, which determine the correspondence between the physical coordinates and image coordinates of the cameras. In this way, the pixel location of both cameras corresponding to a physical point in a light sheet plane is known, although both cameras are not perfectly adjusted to look at same location.

To perform the position calibration, we took images of a calibration plate that had a grid pattern with, for example, 1-mm intervals printed on a light-diffusive glass plate. The surface of the plate was set in the plane of the laser light sheet and illuminated from the back side by a halogen lamp. The grid image was captured by each CCD camera. The locations of individual grid points in the image plane coordinates were automatically obtained by finding local peaks of a cross-correlation function between the grid image and a template image which each had a pattern of one grid. After obtaining the correspondence between the locations of each grid point in the physical coordinate and that in the image coordinate, a third-order polynomial function was fitted by the least-squares method. The image coordinate (X, Y) of the physical coordinate (x, y) was expressed as a function:

$$X = \sum_{i=0}^{3}\sum_{j=0}^{3} \xi_{ij} x^i y^i$$
$$Y = \sum_{i=0}^{3}\sum_{j=0}^{3} \eta_{ij} x^i y^i \qquad (6)$$

Here, the coefficients ξ and η were obtained by the least-square method. This procedure compensated automatically for camera misalignment and distortion due to refraction by the liquid/air interfaces. A similar procedure is discussed in detail by Solof et al. (1997).

3
Application

3.1
Thermal stratified flow

The first example of the technique is an application to a stable thermal stratified pipe flow with plane shear (Sakakibara et al., 1993a).

The higher temperature water at lower velocity flows into the upper settling chamber, and the lower temperature water at high velocity flows into the lower chamber. Both flows pass through the nozzle and form uniform velocity and temperature distributions at the end of the horizontal splitter plate. It then flows through a horizontal Plexiglas pipe of constant diameter $D = 60$ mm for total length of 1640 mm. Cartesian coordinates were adopted with the origin fixed at the trailing edge of the splitter plate. The bulk Reynolds number $Re = U_b D/\nu$ was set at 7400, where U_b denotes a bulk velocity, and ν denotes the kinematic viscosity evaluated at a temperature of the flow in the lower half. The velocities of upper and lower streams U_2, U_1 were 100 and 140 mm/s, respectively. Under the stratified condition, the temperature of the flow in the lower half T_1 was 294 K and the temperature difference (ΔT) between the hot and cold streams was 22 K. The overall Richardson number $Ri = \beta g D \Delta T/(U_1 - U_2)^2$ was 2.5.

Polystyrene particles 5 μm in diameter were used as flow tracers, and 0.5 mgl^{-1} Rhodamine B was dissolved into the working fluid. The test section, shown in Fig. 4, was located at a fixed position near $x/D = 12$. The gradient vector of the mean temperature in the mixing layer was expected to be normal to the horizontal plane. In such a configuration, a laser light sheet passed normal to the plane would not be refracted significantly compared with the light passed along the horizontal plane. Fortunately, no significant fluctuation in light sheet intensity was observed in this study, and thus we did not employ the two-color LIF.

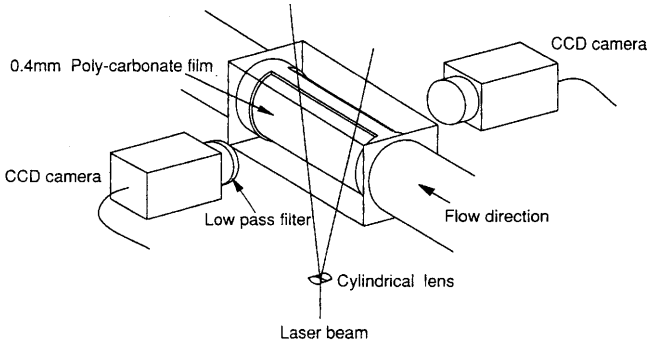

Fig. 4. Schematic view of the test section

Figure 5 shows time-averaged streamwise velocity and turbulent intensities at the location $x/D = 12.3$. A temperature profile at the same location is given in Fig. 6. At this measured position, the mixing layer is fully developed, and it is known that the layer's thickness is constant in this region of a stratified pipe flow (Kobayashi et al. 1990). The local velocity and temperature are normalized by the bulk velocity, U_b, and temperature difference between upper and lower layers, ΔT. The velocity gradient at the center of the pipe is larger for $Ri = 2.5$ than for $Ri = 0$. The minimum velocity is observed in the velocity profile and is located at $y/D = 0.13$ for $Ri = 2.5$, where a strong stratification exists. This is caused by the existence of the minimum velocity in the inlet velocity distributions (Kobayashi et al. 1990). The turbulent intensity also becomes smaller for $Ri = 2.5$ than for the isothermal condition, $Ri = 0$, because the buoyancy force suppresses the mixing. These results are in qualitative agreement with characteristics measured by LDV and thermocouples as reported by Kobayashi et al. (1990).

For understanding the transport of heat, distributions of turbulent heat flux vectors with components of $u'T'$ and $v'T'$ are shown in Fig. 7 with an overlaid temperature map. A crest of the temperature wave (marked as 11) is elongated into an upper layer ($y/D = 0.1$). We call this a 'crest'. Similarly, but in the lower layer, a valley of the wave (marked as 12) is entrained into the lower layer ($y/D = -0.15$). We call this a 'valley'. The elongation of the 'crest' and 'valley' are most likely by a roll-up motion of fluid induced by the mean shear. This flow structure is convected downstream.

It is observed that the 'crest' and 'valley' are associated with downward and upward heat flux vectors, which are a counter-gradient type transfer of heat, marked as 11 and 12. It is considered that the strong heat exchange and momentum transfer occurs near the 'crest' and 'valley'. If the 'crest' and 'valley' flows away from the centerline by roll-up motion, co-gradient type momentum and heat

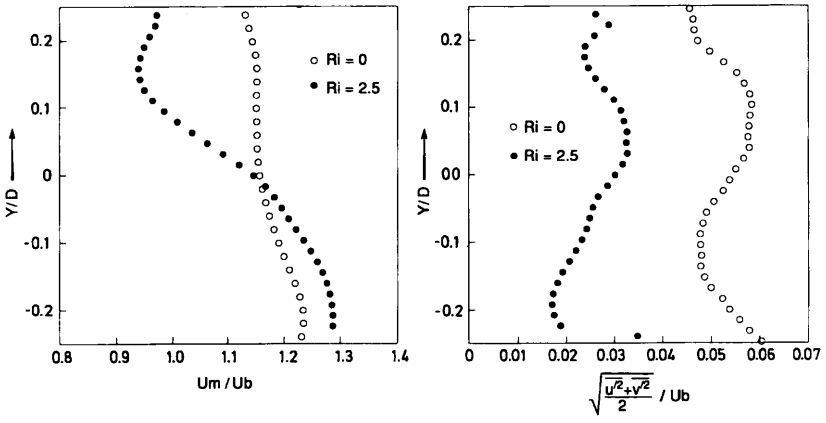

Fig. 5. Distribution of time-averaged streamwise velocity and turbulent intensities at $x/D = 12.3$

transport will become dominant. Nevertheless, the counter-gradient type diffusion will occur, when the 'crest' and 'valley' return to the centerline due to internal motion and presumably buoyancy forces. At the location where the counter-gradient diffusion occurs, the return motion of the 'crest' and 'valley' may be more dominant than that moving away from the centerline. This unbalanced flux of heat and momentum might be caused by the existence of a long internal wave in the pipe.

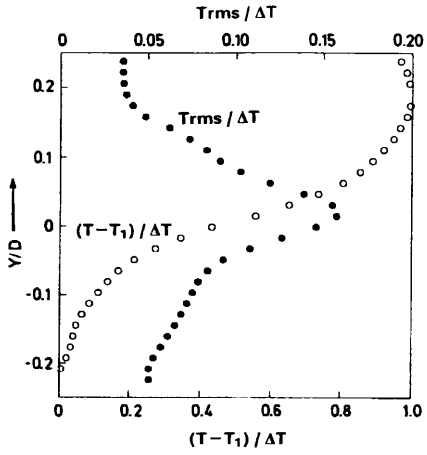

Fig. 6. Distribution of time-averaged temperature and its turbulent intensities at $x/D = 12.3$

3.2
Natural convection

The two-color LIF technique was used to measure the three-dimensional temperature field of thermal convection from a horizontal surface with uniform heating (Sakakibara and Adrian, 1999). The test section consisted of a rectangular box heated from below by electrical mats bonded to the lower side of a smooth 12.7-mm-thick brass plate, as shown in Fig. 8. The box was filled with deionized water with a dye concentration of RhB, $C_{\mathrm{RhB}} = 0.05$ mg/l, and Rh110, $C_{110} = 0.0025$ mg/l. Its interior horizontal dimensions were 152 mm × 381 mm and $H = 40$ mm depth. The top of the fluid layer was a free surface. The mean heat flux supplied by the heater was 27 kW/m^2 and the mean temperature drop from the heated surface to the center of the mixed layer was $\Delta T = 15$ K. The Raleigh number was $Ra = \beta g H^3 \Delta T/\alpha\nu = 1.3 \times 107$, where β is the thermal coefficient of expansion, g is gravity, and α is the thermal diffusivity. To obtain a quasi-three dimensional

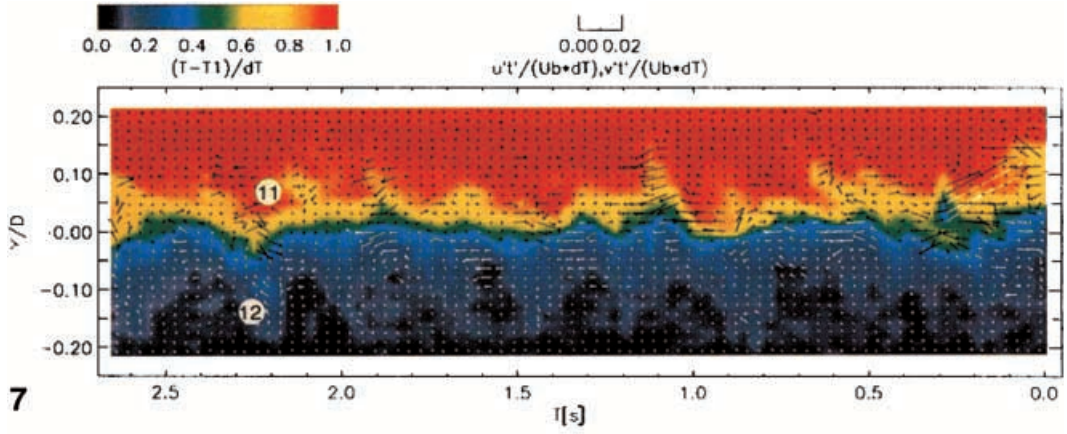

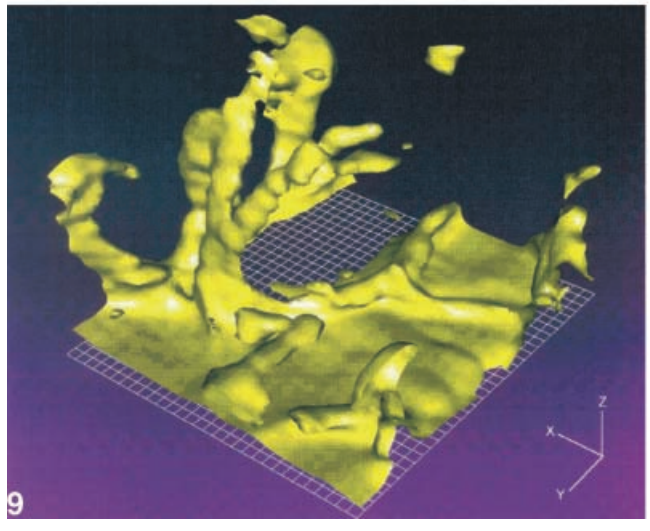

Fig. 7. Temporal variation in heat flux vector under stratified condition
Fig. 9. Surfaces of constant temperature of natural convection

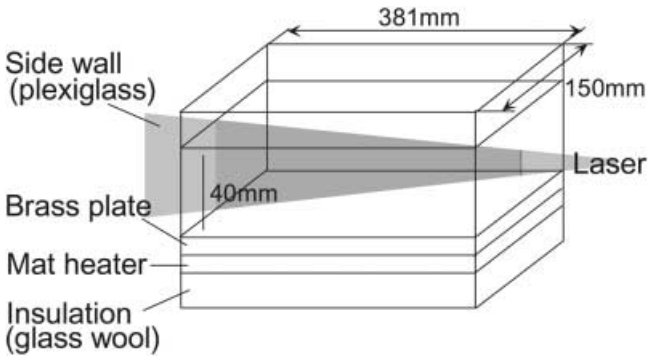

Fig. 8. Experimental apparatus for natural convection

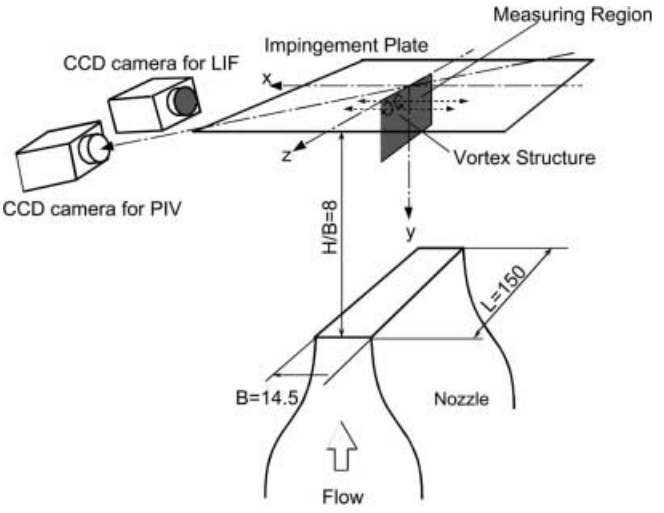

Fig. 10. Test section of plane impinging jet and camera arrangement

reconstruction of the temperature field, the laser light sheet was scanned 30 mm horizontally over a period of 0.73 s. Images were captured every 1/60 s, so the spatial interval of successive images was 0.7 mm. Figure 9 shows surfaces of constant temperature. Here, the white grids represent the horizontal surface and its intervals are 1 mm each. The laser light sheet was parallel to the y-axis and swept in the direction of the x-axis. The flow field was dominated by turbulent structures with the forms of plumes and ridges. The plumes, which consist of columns of buoyant fluid rising up from the thermal boundary layer, are connected to the ridges lying on the surface. These ridges originate from instabilities of the thermal boundary layer at the intersection of the cell, or nodes of the ridges. The temperatures at the nodes are much higher than in other parts of the ridges, or inside the cells. As the fluid inside a cell convects toward the ridges, the hot fluid at the node makes the boundary layer thicker and creates more buoyancy at the node where the plumes rise upwards.

3.3 Impinging jet

The technique has been applied to a plane jet impinging normal to a heated flat surface. It is well known that the high heat transfer rates realized in the stagnation region of turbulent impinging jets have been employed for many practical purposes. For this flow regime, Yokobori et al. (1983) first visualized the counter-rotating vortices normal to the stagnation line on the surface using the hydrogen-bubble technique. Their observations suggest these vortices have a dominant role in turbulent heat transfer at the stagnation region. Instead of their qualitative approach, recent development of our technique has enabled further progress in understanding the thermal and vortical structures of this flow (Sakakibara et al. 1993b, 1996a, b, 1997). In the following sections, we show results for both a plane impinging jet and one with periodic excitation.

3.3.1 Plane impinging jet without excitation

A flow system of our impinging jet is shown schematically in Fig. 10. A water jet issuing upward from a rectangular nozzle impinges on a horizontal, electrically-heated surface. The jet was in the presence of a weak coflowing stream, approximately 5% of the jet centerline velocity, to eliminate recirculating flow and ensure a supply of fluid for jet entrainment. The nozzle exit had a width of $B = 14.5$ mm and an aspect ratio of 10.3. At a spacing H from the jet exit, the jet impinged on a horizontal heated surface. The surface, which had a dimension of 130×145 mm^2, consisted of a 3-mm-thick Bakelite base plate covered with five strips of stainless foil heater. Each stainless foil strip was 30 μm thick and 130×29 mm^2 in area, and was not glued onto the base plate, just in tension to allow the lengthwise thermal expansion of the foil. The strips were electrically connected the d.c. power supply. The jet Reynolds number was set at 2000 and the mean velocity at the nozzle exit was 107 mm/s. The averaged heat flux from the wetted surface of the foil was $q_w = 44$ kW/m^2. The average temperature difference between the surface and fluid was 14.3 K. The x-axis is normal to the symmetry plane of the jet, and y-axis is normal to the plate. The origin is located at a center of the plate.

The laser light sheet illuminated the symmetry plane of the jet and two CCD cameras, one for PIV and the other for PLIF, viewed an area 20×20 mm^2 located near the origin. Since a density gradient induced by a temperature gradient in the thermal boundary layer refracts the light from the object to the camera, the major axis of the CCD camera was tilted at the angle of 22° with respect to the plate to reduce the light path in the boundary layer. Note that the fluctuation of the light sheet intensity due to the refraction was not a serious problem because the light sheet illuminated an area normal to the thermal boundary layer, and thus use of two-color LIF was not needed.

Three successive vector maps in Fig. 11 overlaid on temperature distributions presented in gray scale show a pair of counter-rotating vortices approaching the wall. The fluid at the middle of the vortex pair was ejected out from the boundary layer, and the fluid on either side of the vortex pair was swept toward the wall. We named the former an 'ejection region' and the latter a 'sweep region'. A high temperature layer near the wall is lifted up at the ejection region, and leads on the outer flow. At the sweep region, cold fluid directly impinges to the wall, thinning

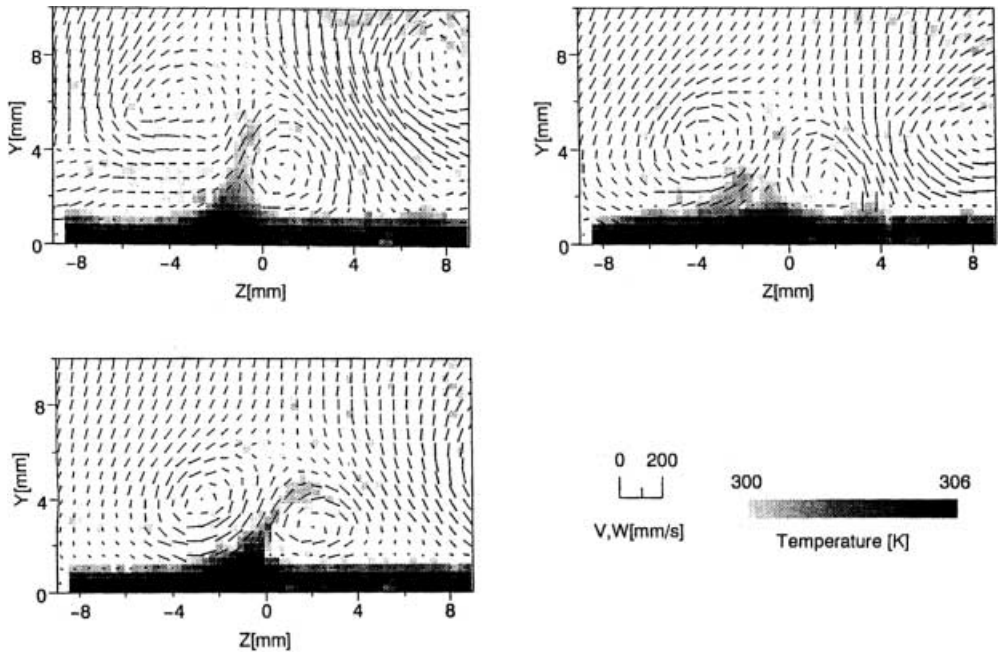

Fig. 11. Instantaneous velocity and temperature above the stagnation line. Time interval of successive maps is 50 ms

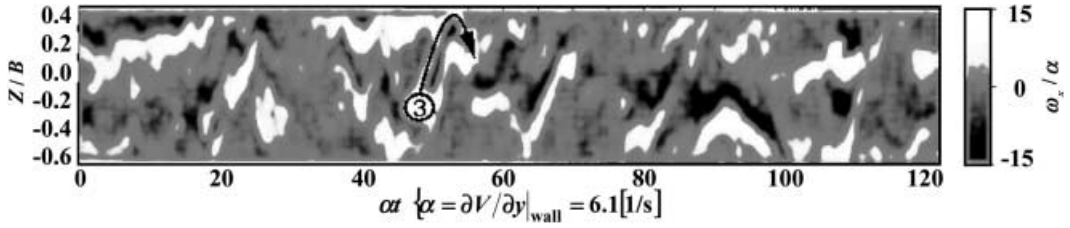

Fig. 12. z–τ diagram of vorticity. Instantaneous vorticity whose absolute value is the maximum in the given z location is plotted

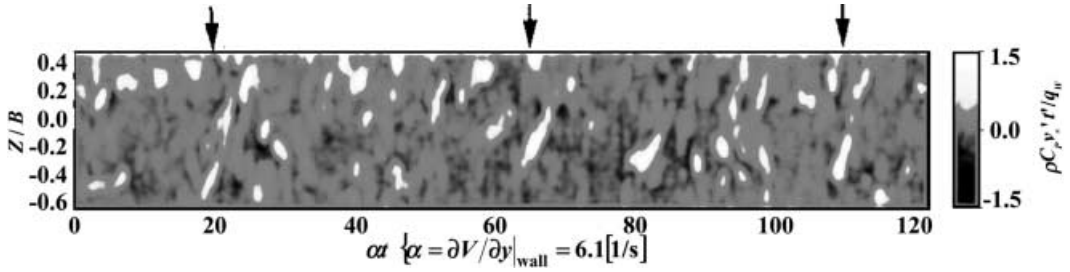

Fig. 13. z–τ diagram of instantaneous turbulent heat flux at $y/B = 0.13$

the boundary layer and sweeping hot fluid toward the center. Finally, the fluid moves away from the wall at the ejection region and is transported to the outer flow.

Figure 12 shows a temporal variation in the x-component of vorticity calculated from hundreds of instantaneous vector maps similar to Fig. 11. In the figure, the instantaneous vorticity, whose absolute value is the maximum in the given z location, is plotted against the time laps τ. This z–τ diagram enables us to see the movement of the vorticity in z-direction. The vortex pairs are sliding or wandering in the z-direction while gradually decreasing their size, but increasing the amplitude of the vorticity. Then finally, it would disappear at some stage and, alternatively, other vortex pairs would appear.

A temporal variation in the instantaneous turbulent heat flux $v't'$ measured at $y/B = 0.13$ is presented in Fig. 13. Several streaks with large heat flux, which are displayed in white, are observed quite intermittently in time and space. Comparing this figure with Fig. 12, one would realize that the location of the streaks exactly matches the location of the middle of the vortex pairs. It is obvious that the ejection of the hot fluid induced by vortex pairs strongly correlates with the generation of the turbulent heat flux.

3.3.2 Plane impinging jet with periodic excitation

As observed in the previous section, the ejection event induced by the vortex pair is quite intermittent and randomly located in space. In such a flow, however, a difficulty might arise in the determination of the coherent motion of such vortices and the generation of the turbulent heat flux, although conditional sampling or several types of orthogonal decomposition schemes have been proposed in the literature. The jet was spatially locked by a fluted nozzle in the vein of mixing layers (Lasheras and Choi 1988). Such locking enabled three-dimensional, three-component phase-averaged vorticity distributions to be determined from a montage of instantaneous two-dimensional PIV slices of the displacement field.

The experimental apparatus is similar to that of the previous section, but modified to add the periodic disturbances as shown in Fig. 14. The streamwise velocity was perturbed by oscillating the spanwise walls of the jet nozzle by two loudspeakers. Since the settling chamber was constructed from 1-mm-thick aluminum, this was achieved by connecting each side wall of the inner settling chamber to the cone of a loudspeaker, which was installed outside the chamber by metal rods. The wave form used to drive the speakers was generated by a PC with a D/A converter board and was supplied after being amplified; it was constructed from two sine waves as

$$V(t) = A_1 \sin 2\pi f_1 t + A_2 \sin(2\pi f_2 + \phi) \qquad (7)$$

where t is time, and the fundamental frequency was set to $f_1 = 3.02$ Hz, which was the natural roll-up frequency of the jet, yielding a Strouhal number $St = 0.36$; the subharmonic frequency was set to $f_2 = f_1/2$. The phase lag f between the two waves was chosen to be $3\pi/4$. The amplitude of each wave was set at the minimum to lock the phase of structures. In addition to the temporal perturbation to the jet, a spatially periodic perturbation was introduced at the exit of the nozzle to fix the spanwise location of any three-dimensional structure that formed downstream. The nozzle edges were fluted with sinusoidal indentations of wavelength λ = 15 mm.

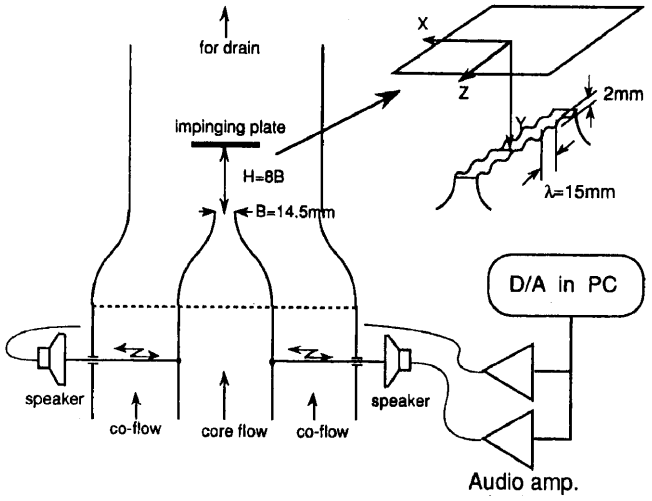

Fig. 14. Impinging jet apparatus with an excitation mechanism

Figure 15 depicts profiles of the mean velocity component V for various nozzle-to-plate spacing H. For both the excited/unexcited condition, V is monotonically increased in magnitude, which is a typical profile of stagnation flow. The gradient is also smaller for an excited case than for that of an unexcited case. For the excited case, the development of the shear layer is much faster, especially near the end of the potential core. Thus the stronger momentum transfer causes more spreading of the jet width and more drop of centerline velocity in a streamwise direction.

The local Nusselt number for various H measured at the stagnation point also showed a clear difference between excited/unexcited cases, as shown in Fig. 16. The Nusselt number is identical for both cases within $H/B < 4$, where the plate was in the potential core of the jet. For increasing distance H, the Nusselt number is gradually increased to a peak at $H/B = 5$ for the excited case and $H/B = 7$ for the unexcited case. The jet excitation, therefore, could reduce the distance H with maximum Nusselt number.

The local maximum of the heat flux, for all variations in H, is measured at approximately $y/B = 0.1$ or closer to the wall. The peak values for the excited/unexcited cases are compared in Fig. 17. As the plate distance H is larger than $6B$, the heat flux for the unexcited case is greater than that of the excited case. It is concluded that the jet excitation could enhances the turbulent heat flux and, therefore, the Nusselt number if the plate distance H is less than $6B$.

The mean momentum equation on the centerline of the jet assuming cross-stream component $U = 0$ is expressed as

$$V\frac{\partial V}{\partial y} = -\frac{\partial P}{\partial y} - \frac{\partial}{\partial x}\overline{u'v'} - \frac{\partial}{\partial y}\overline{v'v'} \qquad (8)$$

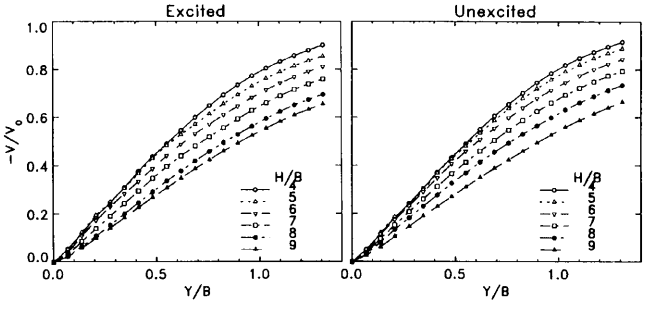

Fig. 15. Streamwise mean velocity profile in the stagnation region

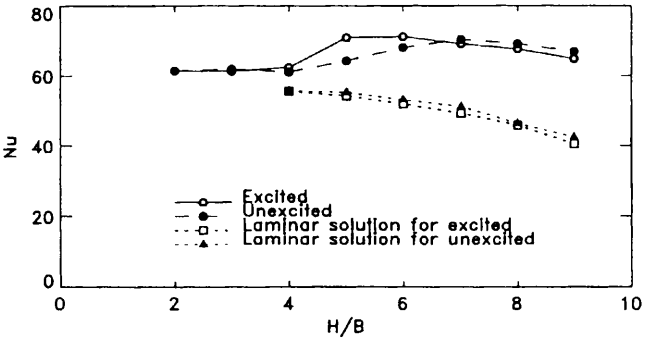

Fig. 16. Nusselt number for various nozzle-plate distances H

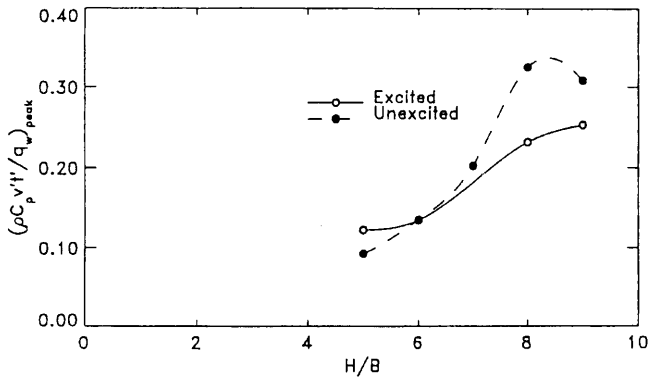

Fig. 17. Maximum turbulent heat flux for various nozzle–plate distances H

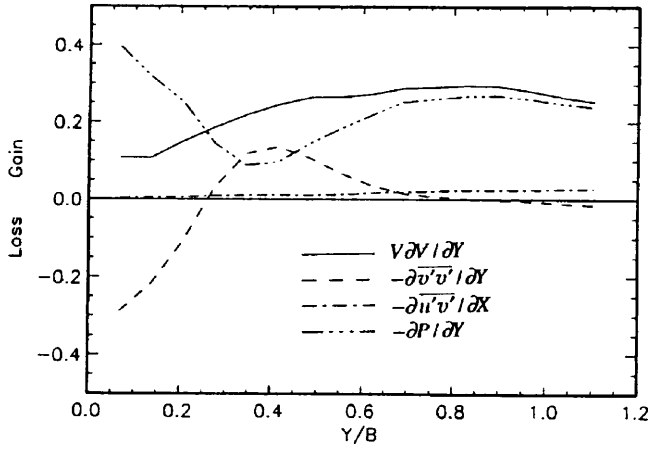

Fig. 18. Budget of momentum equation

where the viscous term was eliminated, since it was much smaller than the other terms. Figure 18 shows variations in each term in Eq. (8) evaluated from the measurement data for $H/B = 8$, excited case. The pressure gradient term was estimated as a residue of all the other terms. At a location apart from the wall, near $y/B = 1$, the convection term is balanced with the pressure term most likely to be the free jet characteristics, while other terms are almost diminished. Near the wall, in turn, the normal stress term is significantly negative. Since the normal stress is, in other words, a measure of the diffusion of V in the y direction, the negative magnitude of this stress contributes to a reduction in the boundary layer thickness.

While the argument presented above is of a statistical issue, the temporal and spatial evolution of the vortical/thermal structures are also quite interesting. We would see phase-averaged structures in the following. Figure 19 depicts a series of phase-averaged velocity distributions with a phase interval of 45°. The light/dark gray shades represent a region where the phase-averaged vorticity is larger/less than a threshold value: 10 1/s. The phase-averaged wall temperature T, velocity component v and normal-strain rate $\partial u/\partial x$ were plotted below each plot. In plot (a), a region with large velocity can be observed at the centerline of the jet with the presence of large-scale spanwise vortices, marked 'A'. Moreover, a descending spanwise vortex, marked 'B', exists in the wall-jet region. Just behind this vortex 'B', the normal-strain rate has a local peak since the fluid near the plate is accelerated and extended by this vortex. This augmentation of normal strain rate causes the following two effects. One is a stretching of the streamwise-counter-rotating vortices. This fact can be interpreted as a positive value of v' where the roller B is located, and a generation of the turbulent heat flux can be expected. The other is a surface renewal effect of the thermal boundary layer. The normal straining of fluid near the wall reduces the thickness of the local boundary layer and thus more heat flux is realized instantaneously. By these two effects, the local wall temperature under the vortex is suddenly decreased after passage of the vortex, and such a temperature distribution propagates with a convecting vortex; it is obvious to see the movement of 'B' in the series b–d and the corresponding wall-temperature distribution.

As we shall determine in the following section, a seed of the counter-rotating vortices exists in a spanwise roller. So the spanwise roller accompanies the counter-rotating vortices toward the wall, and then increases the velocity component v', which is an indication of the vorticity of the counter-rotating vortices.

The seed of the counter-rotating vortices, as mentioned previously, could successfully be visualized in a three-dimensional view of the phase-averaged vorticity iso-surfaces, depicted in Fig. 20. To obtain three-dimensional volumetric data from two-dimensional PIV data, we divided the measurement volume into 85 slices; 33 x–y, 32 y–z and 20 x–z planes. A single CCD camera and a laser light sheet were arranged as shown in Fig. 21 and then performed PIV measurement for each slice separately in time. Although the measurement for whole volume was not perform simultaneously, the phase-averaged velocity/vorticity data are expected to reveal the 'instantaneous' coherent structures in such a low Reynolds number, well-phase-locked velocity field. The calibration of an image coordinate into a physical coordinate was carefully done; three laser light beams crossing in orthogonally at one point were mounted on a three-dimensional computer-controlled traverse mechanism. The crossing point was moved to four 'known' positions in a laser sheet plane, and the pixel position of the crossing point in its captured image was manually picked up. The calibration scheme, presented in the previous section, was then applied to calculate a mapping function between physical- and image-coordinate.

In Fig. 20 the meshed plane surface represents the impinging plate, the meshed gray surface is of the z-component (spanwise) of vorticity, the dark and light gray surfaces are of the y- and x-components of vorticity. In Fig. 20a, the rib vortices, whose axis is about normal to the plate, are presented between the spanwise roller. These ribs are connected to the outer side of the successive, or upstream, rollers, as shown in Fig. 20b. The spanwise roller has sinusoidal distortion, which was originally induced by the spanwise periodic disturbance added by sinusoidal indentations of the nozzle. This distortion becomes even stronger, and rollers are broken up into three portions after passing the impingement region (in Fig. 20b). The counter-rotating vortices are clearly iden-

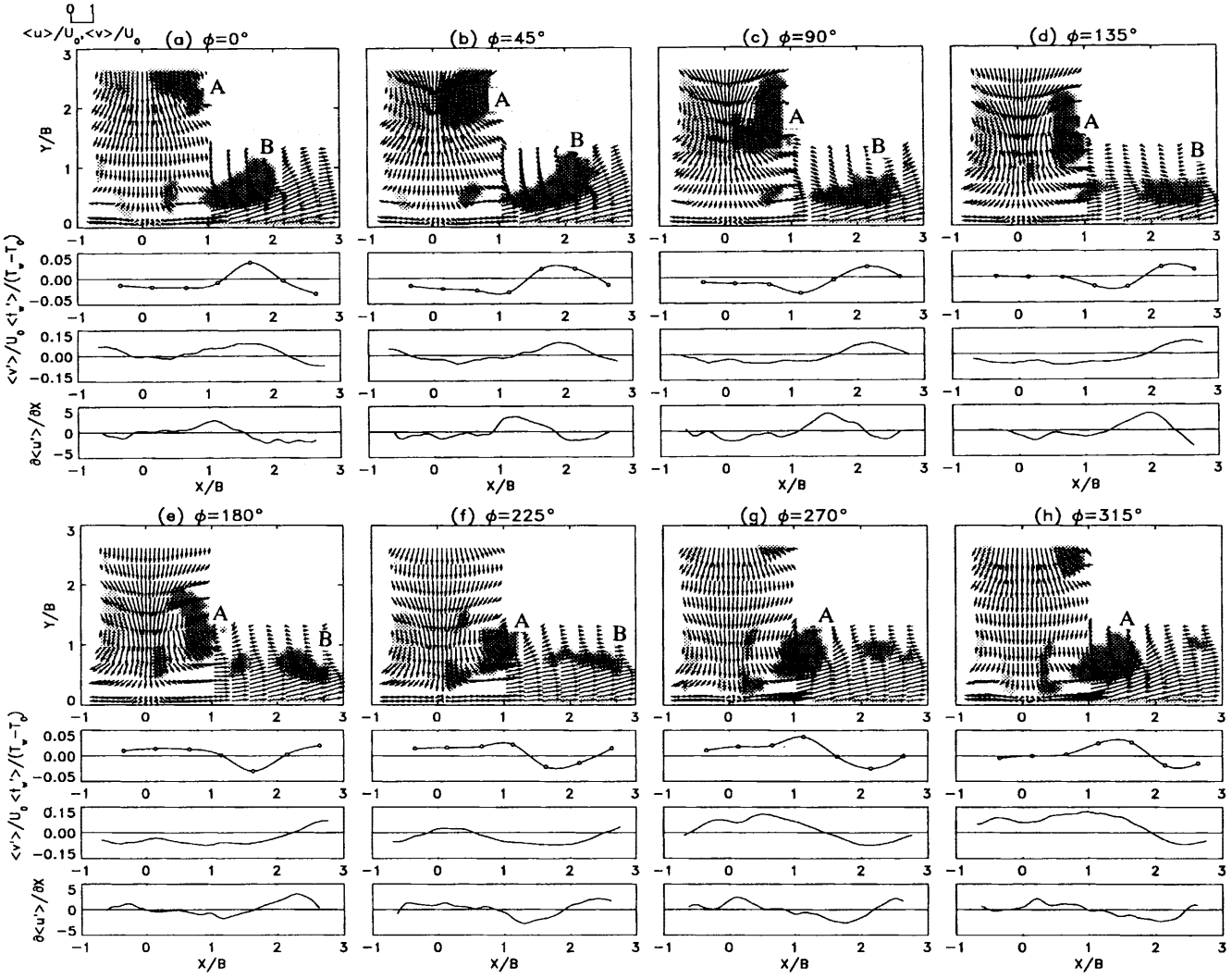

Fig. 19. Evolution of the phase-averaged velocity/vorticity maps. Wall temperature, velocity component normal to the wall, v, and rate of strain are shown below each map

tified as light gray surfaces of streaks on the plate. Furthermore, we would like to emphasize the vortex portion, indicated as CR in Fig. 20a, presented between spanwise rollers. This vortex portion, which actually merges together with the existing counter-rotating vortices on the plate, is the seed of counter-rotating vortices as mentioned previously. The counter-rotating vortices are then stretched, so that the vorticity might be amplified to conserve angular momentum. Further details of the structures are presented in Sakakibara et al. (2000).

4
Concluding remarks

We have presented a new technique for measuring the turbulent heat flux based on the simultaneous use of PIV and PLIF to measure both velocity and temperature. Fluorescent dye and tracer particles are mixed in the flow, and two CCD cameras, one for PLIF and the other for PIV, are used at a same time to capture both the fluorescence and particle images. This combined technique has been applied to clarify the heat transfer and turbulent characteristics of stratified flow, natural convection and plane impinging jet.

Measurements of velocity and temperature in the thermal stratified flow in a horizontal pipe showed that the colder bulk water entrained into the hot layer is recognized as a 'crest' and the hot water entrained into the cold layer as a 'valley'. They are located above and below the centerline, and were elongated backwards and forwards respectively. The instantaneous distributions of the heat vectors and temporal variation in temperature showed a strong exchange of heat and momentum occurring through the 'crest' and 'valley'. Instantaneous co-gradient and counter-gradient types of diffusion of heat and momentum have been recognized in those structures.

In the natural convection over a horizontal heated surface, the two-color PLIF was adopted to measure the three-dimensional structure of temperature. The temperatures at a the nodes are much higher than in other parts of the ridges or inside the cells. As the fluid inside a cell convects toward the ridges, the accumulation of the heat at

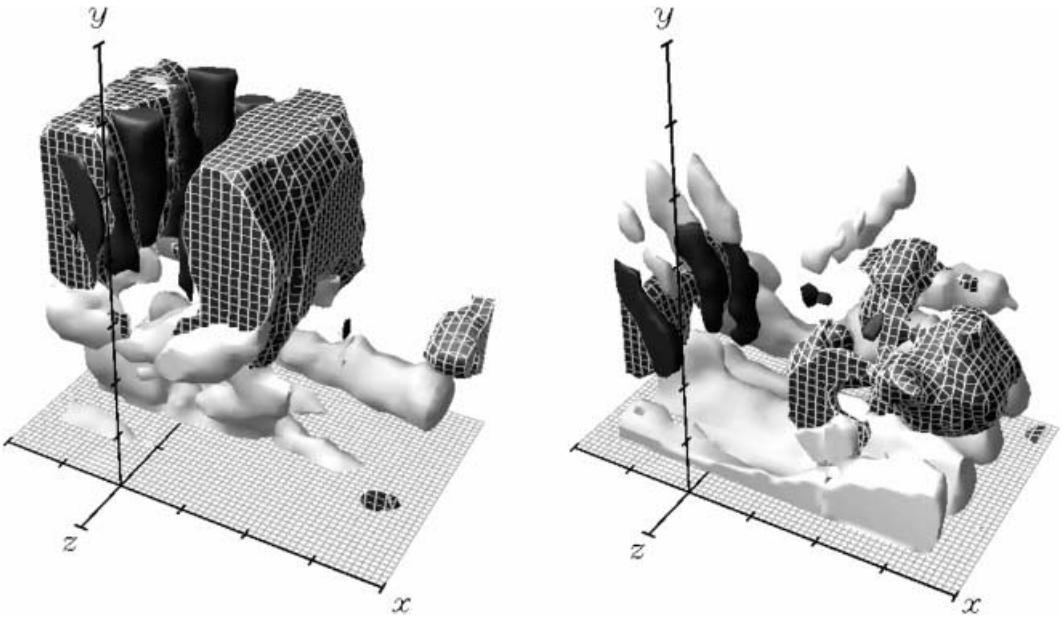

Fig. 20. Surfaces of constant phase-averaged vorticity in the stagnation region

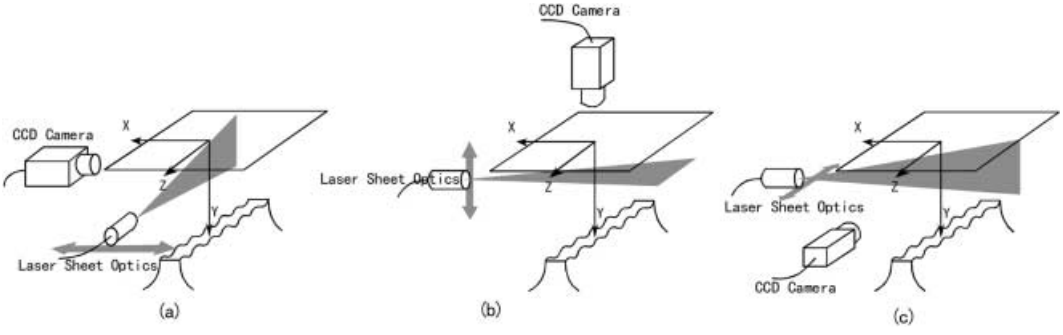

Fig. 21. Arrangement of cameras for measuring the data in Fig. 20

the node makes the boundary layer thicker and creates more buoyancy at the node where the plumes rise upwards.

The application of the present technique to the impinging plane jet clarified many new aspects of that flow. The ejection and sweep induced by counter-rotating vortices in the stagnation region contribute significantly to the generation of turbulent heat flux from the surface. The jet excitation was applied to enhance and control the flow and heat transfer. Since the jet excitation could enhance the momentum transfer and the activity of the counter-rotating vortices, the heat transfer rate could be augmented when the impingement plate was set at $H/B = 5$–6. The 'seed' of the counter-rotating vortices are observed in the middle of the spanwise roller. Whenever the spanwise roller approaches toward the plate, the seed vortices merge into the counter-rotating vortices, and vortex stretching induced by the mean strain amplifies the vorticity of these vortices.

The results obtained above are only available if one uses a whole field measurement such as a PIV, PLIF technique. We are quite optimistic for the further growth of research activity concerning flow measurement using the techniques presented here.

References

Akino N; Kunugi T; Ueda M; Kurosawa A (1988) Liquid-crystal thermometry based on automatic color evaluation and applications to measure turbulent heat transfer. In: Hirata M, Kasagi N (eds) Transport phenomena in turbulent flows theory, experiment and numerical. Hemisphere, London, simulation pp 807–820

Arbeloa TL; Estevez MJT; Arbeloa FL; Aguirresacona IU; Arbeloa IL (1991) Luminescence properties of rhodamines in water/ethanol mixtures. J Lumin 48/49: 400–404

Dabiri D; Gharib M (1991) Digital particle image thermometry: the method and implementation. Exp Fluids 11: 77–86

Dahm WJA; Southerland KB; Buch KA (1991) Direct, high-resolution, four-dimensional measurements of the fine scale structure of Sc $\gg$1 molecular mixing in turbulent flows. Phys Fluids A 3: 1115

Dahm WJA; Su LK; Southerland KB (1992) A scalar imaging velocimetry technique for fully resolved four-dimensional vector velocity field measurement in turbulent flows. Phys Fluids A 4: 2191

Fujisawa N; Adrian RJ; Keane RD (1997) Three-dimensional temperature measurement in turbulent thermal convection over smooth and rough surfaces by scanning liquid crystal

thermometry. Proc Int Conf on Fluid Engineering, JSME Centennial Grand Congress, Tokyo, pp 1037–1042
Hanson RK (1986) Combustion diagnostics: planar imaging techniques. 21st Symp (Int) on Combustion, The Combustion Institute, Pittsburgh, pp 1677–1691
Joklik RG; Horvath JJ; Semerjian HG (1991) Temperature measurements in flames using thermally assisted laser-induced fluorescence of Ga. Appl Optics 30: 1497–1504
Kobayashi K; Hishida K; Maeda M (1990) Turbulent transport across stable thermal stratified layer in a circular pipe. Proc 9th Int Heat Transfer Conf, Jerusalem, vol 5, pp 341–346
Jones G II (1990) Photochemistry of laser dyes. In: Duarte FJ, Hillman LW (eds) Dye laser principles with applications. Academic Press, New York, pp 287–343
Lasheras JC; Choi H (1988) Three-dimensional instability of a plane free shear layer: an experimental study of the formation and evolution of streamwise vortices. J Fluid Mech 189: 53–86
Nakajima T; Utsunomiya M; Ikeda Y; Matsumoto R (1990) Simultaneous measurement of velocity and temperature of water using LDV and fluorescence technique. 5th Int Symp on Appl Laser Tech to Fluid Mech, Lisbon, 2.6.1–2.6.6
Sakakibara J; Hishida K; Maeda M (1993a) Measurements of thermally stratified pipe flow using image-processing techniques. Exp Fluids 16: 82–96
Sakakibara J; Hishida K; Maeda M (1993b) Quantitative visualization of convective heat transfer near the stagnation region of an impinging jet. Exp Numer Flow Visualization, ASME FED-172, 93–99
Sakakibara J; Hishida K; Maeda M (1996a) Vortex structure in the stagnation region of an excited plane impinging. Trans JSME 62–596: 1369–1376
Sakakibara J; Hishida K (1996b) Heat transfer in the stagnation region of an excited plane impinging jet. Trans JSME 62–597: 1962–1969
Sakakibara J; Hishida K; Maeda M (1997) Vortex structure and heat transfer in the stagnation region of an impinging plane jet. Int J Heat Mass Transfer 40: 3163–3176
Sakakibara J; Adrian RJ (1999) Whole field measurement of temperature in water using two-color laser induced fluorescence. Exp Fluids 26: 7–15
Sakakibara J; Hishida K; Phillips WRC (2000) On the vortical structure in a plane impinging jet. TAM Report No. 933, UILU-ENG-2000-6008, University of Illinois at Urbana Champaign
Sato K; Kasagi N; Suzuki Y (1997) Combined velocity and scalar field measurement with the simultaneous use of PIV and scanning LIF. Proc 10th Int Symp Transport Phenomena in Thermal Science and Process Engineering, Kyoto, vol. 2, pp 541–546
Solof S; Adrian RJ; Liu Z (1997) Distortion compensation for generalized stereoscopic particle image velocimetry. Meas Sci Technol 8: 1441–1454
Yokobori S; Kasagi N; Hirata M (1983) Transport phenomena at the stagnation region of a two-dimensional impinging jet. Trans JSME B 49(441): 1029–1039